Non-linear Compensator for handling non-linear Effects in EGR VGT Diesel Engines

Johan Wahlström and Lars Eriksson

Vehicular systems
Department of Electrical Engineering
Linköpings universitet, SE-581 83 Linköping, Sweden
WWW: www.vehicular.isy.liu.se
E-mail: {johwa, larer}@isy.liu.se
Report: LiTH-ISY-R-2897

April 30, 2009

Abstract

A non-linear compensator is investigated for handling of non-linear effects in diesel engines. This non-linear compensator is a non-linear state dependent input transformation that is developed by inverting the models for EGR-flow and turbine flow having actuator position as input and flow as output. The non-linear compensator is used in an inner loop in a control structure for coordinated control of EGR-fraction and oxygen/fuel ratio. A stability analysis of the open-loop system with a non-linear compensator shows that it is unstable in a large operating region. This system is stabilized by a control structure that consists of PID controllers and min/max-selectors. The EGR flow and the exhaust manifold pressure are chosen as feedback variables in this structure. Further, the set-points for EGR-fraction and oxygen/fuel ratio are transformed to set-points for the feedback variables. In order to handle model errors in this set-point transformation, an integral action on oxygen/fuel ratio is used in an outer loop. Experimental validations of the proposed control structure show that it handles nonlinear effects, and that it reduces EGR-errors but increases the pumping losses compared to a control structure without non-linear compensator.

Contents

1 Introduction

Legislated emission limits for heavy duty trucks are constantly reduced. To fulfill the requirements, technologies like Exhaust Gas Recirculation (EGR) systems and Variable Geometry Turbochargers (VGT) have been introduced. The primary emission reduction mechanisms utilized to control the emissions are that NO_x can be reduced by increasing the intake manifold EGR-fraction x_{egr} and smoke can be reduced by increasing the air/fuel ratio [4]. Note that exhaust gases, present in the intake, also contain oxygen which makes it more suitable to define and use the oxygen/fuel ratio λ_O instead of the traditional air/fuel ratio. The main motive for this is that it is the oxygen contents that is crucial for smoke generation. Besides λ_O it is natural to use EGR-fraction x_{egr} as the other main performance variable, but one could also use the burned gas fraction instead of the EGR-fraction.

The oxygen/fuel ratio λ_O and EGR fraction x_{egr} depend in complicated ways on the EGR and VGT actuation. It is therefore necessary to have coordinated control of the EGR and VGT to reach the legislated emission limits in NO_x and smoke. Various approaches for coordinated control of the EGR and VGT for emission abatement have been published. [3] presents a good overview of different control aspects of diesel engines with EGR and VGT, and in [9] there is a comparison of some control approaches with different selections of performance variables. Other control approaches are described in [2], [8], [12], [1], and [11].

Inspired by an approach in [5], a non-linear compensator is investigated for handling of non-linear effects in diesel engines. This non-linear compensator is a non-linear state dependent input transformation that is developed by inverting the models for EGR-flow and turbine flow having actuator position as input and flow as output. The non-linear compensator is used in an inner loop and a control structure with PID controllers and min/max-selectors similar to [13] is used in an outer loop. The control objectives for the control structure are described in Sec. 1.1. Sec. 2 describes a mean value diesel engine model that is first used for system analysis in Sec. 3 and later used for development and analysis of the non-linear compensator and the proposed control structure. The control structure in [13] is described in Sec. 4. The non-linear compensator is developed and analyzed in Sec. 5, while Sec. 6 describes a control structure with non-linear compensator. The control structure in [13] and the proposed control structure are compared in an engine test cell in Sec. 7.

1.1 Control objectives

The primary variables to be controlled are normalized oxygen/fuel ratio λ_O, intake manifold EGR-fraction x_{egr}, engine torque M_e, and turbocharger speed n_t. The goal is to follow a driving cycle while maintaining low emissions, low fuel consumption, and suitable turbocharger speeds, which gives the following control objectives for the performance variables.

1. λ_O should be greater than a soft limit, a set-point λ_O^s, which enables a trade-off between emission, fuel consumption, and response time.

2. λ_O is not allowed to go below a hard minimum limit λ_O^{min}, otherwise there will be too much smoke. λ_O^{min} is always smaller than λ_O^s.

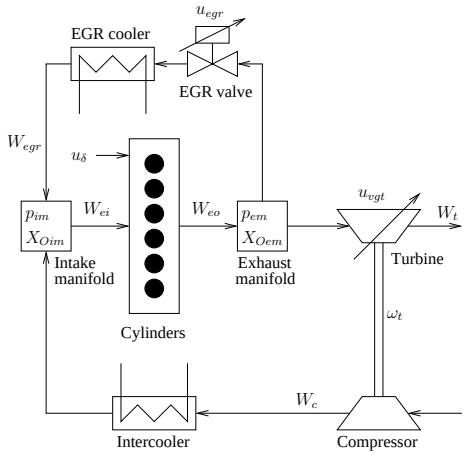

Figure 1: Sketch of the diesel engine model used for system analysis and control design. It has five states related to the engine (p_{im}, p_{em}, X_{Oim}, X_{Oem}, and ω_t) and three for actuator dynamics.

3. x_{egr} should follow its set-point x^s_{egr}. There will be more NO_x if the EGR-fraction is too low and there will be more smoke if the EGR-fraction is too high.

4. The engine torque, M_e, should follow the set-point M^s_e from the drivers demand.

5. The turbocharger speed, n_t, is not allowed to exceed a maximum limit n^{max}_t, preventing turbocharger damage.

6. The pumping losses, M_p, should be minimized in stationary points in order to decrease the fuel consumption.

The aim is now to develop a control structure that achieves all these control objectives when the set-points for EGR-fraction and engine torque are reachable.

2 Diesel engine model

A model for a heavy duty diesel engine is used for system analysis and control design. This diesel engine model is focused on the gas flows, see Fig. 1, and it is a mean value model with eight states: intake and exhaust manifold pressures (p_{im} and p_{em}), oxygen mass fraction in the intake and exhaust manifold (X_{Oim} and X_{Oem}), turbocharger speed (ω_t), and three states describing the actuator dynamics for the two control signals (u_{egr} and u_{vgt}) where there are two states for the EGR-actuator to describe an overshoot. These states are collected in a state vector x

$$x = [p_{im} \quad p_{em} \quad X_{Oim} \quad X_{Oem} \quad \omega_t \quad \tilde{u}_{egr1} \quad \tilde{u}_{egr2} \quad \tilde{u}_{vgt}]^T$$

There are no state equations for the manifold temperatures, since the pressures and the turbocharger speed govern the most important system properties,

such as non-minimum phase behaviors, overshoots, and sign reversals, while the temperature states have only minor effects on these system properties.

The resulting model is expressed in state space form as

$$\dot{x} = f(x, u, n_e)$$

where the engine speed n_e is considered as an input to the model, and u is the control input vector

$$u = [u_\delta \quad u_{egr} \quad u_{vgt}]^T$$

which contains mass of injected fuel u_δ, EGR-valve position u_{egr}, and VGT actuator position u_{vgt}.

A detailed description and derivation of the model together with a model tuning and a validation against test cell measurements is given in [15]. The derivatives of the engine state variables are given by (1), the dynamics of the actuators is given by (2)–(5), and the oxygen concentration in the exhaust gas is calculated in (6). Further, the main performance variables are defined by (7), the EGR flow model is given by (8)–(11), and the turbine flow model is given by (12)–(14).

$$\frac{d}{dt} p_{em} = f_1(x, u), \quad \frac{d}{dt} \omega_t = f_2(x, u) \tag{1a}$$

$$\frac{d}{dt} p_{im} = \frac{R_a T_{im}}{V_{im}} (W_c + W_{egr} - W_{ei}) \tag{1b}$$

$$\frac{d}{dt} X_{Oim} = \frac{R_a T_{im}}{p_{im} V_{im}} ((X_{Oem} - X_{Oim}) W_{egr} + (X_{Oc} - X_{Oim}) W_c) \tag{1c}$$

$$\frac{d}{dt} X_{Oem} = \frac{R_e T_{em}}{p_{em} V_{em}} (X_{Oe} - X_{Oem}) (W_f + W_{ei}) \tag{1d}$$

$$\tilde{u}_{egr} = K_{egr} \tilde{u}_{egr1} - (K_{egr} - 1)\tilde{u}_{egr2} \tag{2}$$

$$\frac{d}{dt} \tilde{u}_{egr1} = \frac{1}{\tau_{egr1}} (u_{egr}(t - \tau_{degr}) - \tilde{u}_{egr1}) \tag{3}$$

$$\frac{d}{dt} \tilde{u}_{egr2} = \frac{1}{\tau_{egr2}} (u_{egr}(t - \tau_{degr}) - \tilde{u}_{egr2}) \tag{4}$$

$$\frac{d}{dt} \tilde{u}_{vgt} = \frac{1}{\tau_{vgt}} (u_{vgt}(t - \tau_{dvgt}) - \tilde{u}_{vgt}) \tag{5}$$

$$X_{Oe} = \frac{W_{ei} X_{Oim} - W_f (O/F)_s}{W_f + W_{ei}} \tag{6}$$

$$x_{egr} = \frac{W_{egr}}{W_c + W_{egr}}, \quad \lambda_O = \frac{W_{ei} X_{Oim}}{W_f (O/F)_s} \tag{7}$$

$$W_{egr} = \frac{A_{egrmax} f_{egr}(\tilde{u}_{egr}) p_{em} \Psi_{egr}}{\sqrt{T_{em} R_e}} \tag{8}$$

$$\Psi_{egr} = 1 - \left(\frac{1 - \Pi_{egr}}{1 - \Pi_{egropt}} - 1 \right)^2 \tag{9}$$

$$\Pi_{egr} = \begin{cases} \Pi_{egropt} & \text{if } \frac{p_{im}}{p_{em}} < \Pi_{egropt} \\ \frac{p_{im}}{p_{em}} & \text{if } \Pi_{egropt} \leq \frac{p_{im}}{p_{em}} \leq 1 \\ 1 & \text{if } 1 < \frac{p_{im}}{p_{em}} \end{cases} \tag{10}$$

$$f_{egr}(\tilde{u}_{egr}) = \begin{cases} c_{egr1}\,\tilde{u}_{egr}^2 + c_{egr2}\,\tilde{u}_{egr} + c_{egr3} & \text{if } \tilde{u}_{egr} \leq \frac{-c_{egr2}}{2\,c_{egr1}} \\ c_{egr3} - \frac{c_{egr2}^2}{4\,c_{egr1}} & \text{if } \tilde{u}_{egr} > \frac{-c_{egr2}}{2\,c_{egr1}} \end{cases} \tag{11}$$

$$W_t = \frac{A_{vgtmax}\,p_{em}\,f_{\Pi t}(\Pi_t)\,f_{vgt}(\tilde{u}_{vgt})}{\sqrt{T_{em}\,R_e}} \tag{12}$$

$$f_{\Pi t}(\Pi_t) = \sqrt{1 - \Pi_t^{K_t}}, \quad \Pi_t = \frac{p_{amb}}{p_{em}} \tag{13}$$

$$f_{vgt}(\tilde{u}_{vgt}) = c_{f2} + c_{f1}\sqrt{\max\left(0, 1 - \left(\frac{\tilde{u}_{vgt} - c_{vgt2}}{c_{vgt1}}\right)^2\right)} \tag{14}$$

3 System properties

An analysis of the characteristics and the behavior of a system aims at obtaining insight into the control problem. This is known to be important for a successful design of a EGR and VGT controller due to non-trivial intrinsic properties, see for example [7]. Therefore, a system analysis of the model in Sec. 2 is performed in [16]. The analysis shows that the DC-gains for the channels $u_{vgt} \rightarrow \lambda_O$, $u_{egr} \rightarrow \lambda_O$, and $u_{vgt} \rightarrow p_{em}$ change sign with operating point.

3.1 Mapping of sign reversal

Knowledge about the sign reversal in the entire operating region is important when developing a control structure. Therefore, the sign reversal is mapped in [16] by simulating step responses in the entire operating region. In Fig. 2 the sign reversals in $u_{vgt} \rightarrow \lambda_O$, $u_{egr} \rightarrow \lambda_O$, and $u_{vgt} \rightarrow p_{em}$ are mapped by calculating the DC-gain in the step responses and then plotting the contour line where the DC-gain is equal to zero. The step responses are simulated at 20 different u_{vgt} points, 20 different u_{egr} points, 3 different n_e points, and 3 different u_δ points. The size of the steps in u_{vgt} is 5% of the difference between two adjoining operating points. A system analysis also shows that the engine frequently operates in operating points where the sign reversal occurs for the channels $u_{vgt} \rightarrow \lambda_O$ and $u_{vgt} \rightarrow p_{em}$ [16]. Consequently, it is important to consider the sign reversal for $u_{vgt} \rightarrow \lambda_O$ and $u_{vgt} \rightarrow p_{em}$ in the control design.

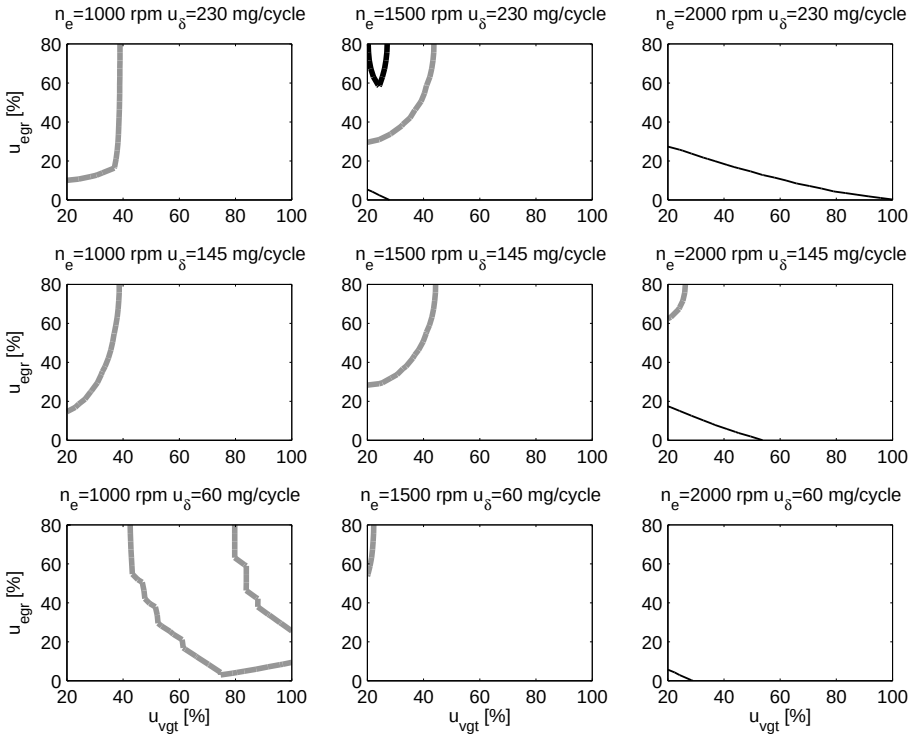

Figure 2: For the system in Sec. 2, the channel $u_{vgt} \rightarrow \lambda_O$ has a sign reversal (thick gray line) that occurs at low to medium engine speed, $u_{egr} \rightarrow \lambda_O$ has a sign reversal (thin black line) that occurs at high engine speed, and $u_{vgt} \rightarrow p_{em}$ has a sign reversal (thick black line) that occurs at a small region with high load and medium engine speed.

4 Control structure with PID controllers

A control structure with PID controllers and min/max-selectors is proposed in [13] with the following algorithm

$$u_{egr}(t_i) = \begin{cases} \min\left(-\mathrm{PI}_1(e_{\lambda_O}), \\ \mathrm{PI}_2(e_{xegr})\right) & \text{, if } u_{vgt}(t_{i-1}) = 100 \\ \\ -\mathrm{PI}_1(e_{\lambda_O}) & \text{, else} \end{cases} \tag{15}$$

$$u_{vgt}(t_i) = \begin{cases} 100 & \text{, if } (u_{vgt}(t_{i-1}) = 100) \\ & \quad \& \, (e_{xegr} < 0.01) \\ \\ \max\left(-\mathrm{PI}_3(e_{xegr}), \right. \\ \left. -\mathrm{PID}_4(e_{nt})\right) & \text{, else} \end{cases} \tag{16}$$

where $e_{\lambda_O} = \lambda_O^s - \lambda_O$, $e_{xegr} = x_{egr}^s - x_{egr}$, and $e_{nt} = n_t^s - n_t$. This structure handles the sign reversal in $u_{vgt} \rightarrow \lambda_O$ because u_{egr} is used to control λ_O, and it also minimizes the pumping work by opening the EGR-valve and the VGT as much as possible while achieving the control objectives for λ_O and x_{egr} [13].

4.1 Engine test cell experiments

The control structure (15)–(16) is applied and validated in an engine test cell. The goal is to experimentally verify the control performance during steps in λ_O^s.

An available production observer, similar to the one in [10], is used to estimate the oxygen mass fraction X_{Oim}. Once X_{Oim} is estimated, the mass flow into the engine W_{ei}, λ_O and x_{egr} are calculated. The engine speed (n_e), intake and exhaust manifold pressure (p_{im}, p_{em}) and turbocharger speed (n_t) are measured with production sensors. Due to measurement noise, all measured and observed variables are filtered using low pass filters with a time constant of 0.1 s. The PID parameters are initially tuned using the method in [14] with $\gamma_{Me} = 3/2$ and $\gamma_{egr} = 1/2$, and are then manually fine tuned in the engine test cell experiments. The experiment in Fig. 3 shows that the control structure (15)–(16) gives slow control at the first step and oscillations at the third step. This is due to that the DC-gains in $u_{egr} \rightarrow \lambda_O$ and $u_{vgt} \rightarrow x_{egr}$ (the two loops that are used as feedbacks in (15)–(16)) increase when λ_O increases. This could be handled using gain scheduling, but it is time consuming to tune the parameters for each operating point. Instead, these non-linear effects are handled using a non-linear compensator that will be described in the following sections.

5 Non-linear compensator

To handle the sign reversal in $u_{vgt} \rightarrow \lambda_O$ and $u_{vgt} \rightarrow p_{em}$ in Fig. 2 and the non-linear effects in Fig. 3, a non-linear compensator is used according to Fig. 4. This non-linear compensator is a non-linear state dependent input transformation that is developed by inverting the models for EGR-flow and turbine flow having actuator position as input and flow as output. The approach is similar to [5] that performs these inversions on similar models for EGR-flow and turbine flow. These inversions lead to two new control inputs, $u_{W_{egr}}$ and u_{W_t}, which are the EGR-flow W_{egr} and the turbine flow W_t provided there are no model errors in the non-linear compensator.

In the following sections, the non-linear compensator is described and the system properties of the system in Fig. 4 are investigated. In Sec. 5.1 only the non-linear compensator for the EGR-actuator is considered according to Fig. 5 and in Sec. 5.2 the non-linear compensator for both the EGR and VGT-actuator is considered according to Fig. 4.

5.1 Inversion of position to flow model for EGR

The non-linear compensator in Fig. 5 is a static inversion of the EGR-flow model (8) to (11) having actuator position as input and flow as output. This inversion results in the following expressions for u_{egr} with $u_{W_{egr}}$ as a new control input

$$f_{egr} = \frac{u_{W_{egr}} \sqrt{T_{em}\, R_e}}{A_{egrmax}\, p_{em}\, \max(\Psi_{egr}, 0.1)} \tag{17}$$

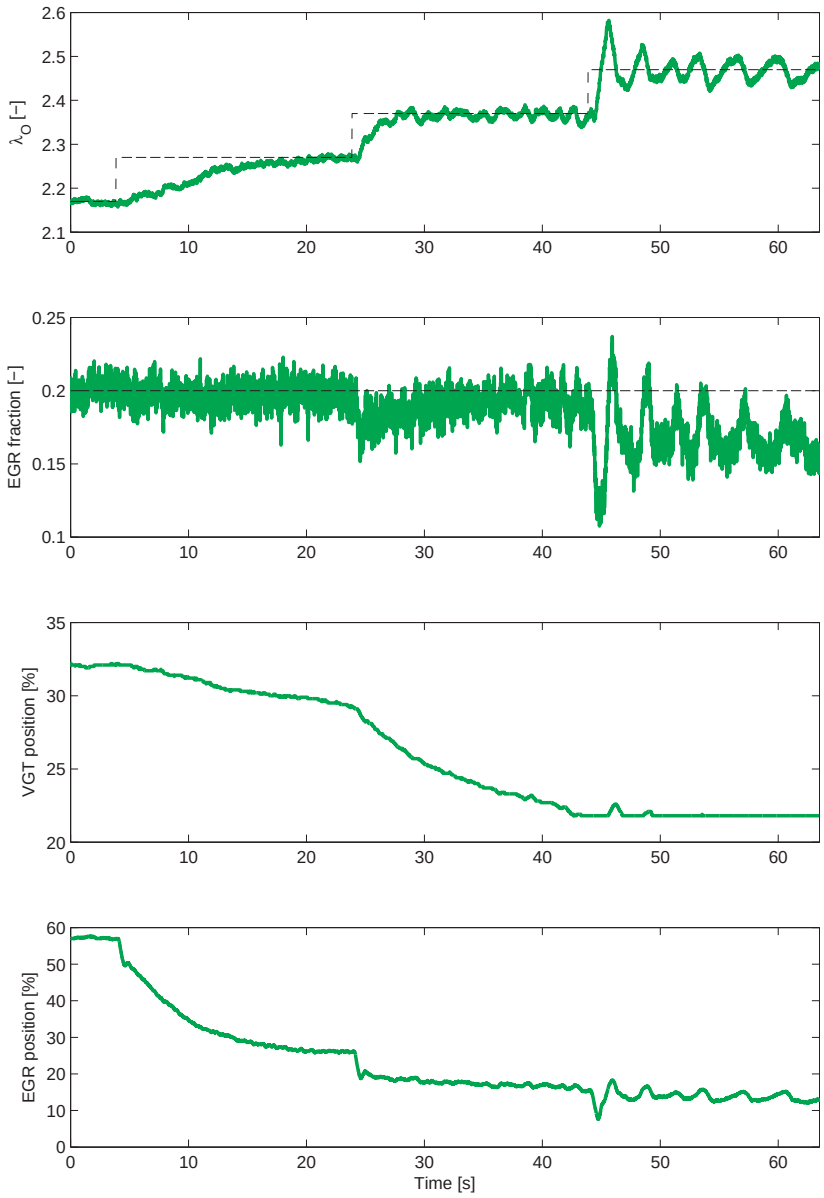

Figure 3: Step responses for the control structure (15)–(16) in an engine test cell showing slow control and oscillations at different steps, i.e. this control structure does not handle non-linear effects in the diesel engine. Operating point: $n_e = 1200$ rpm and $u_\delta = 136$ mg/cycle.

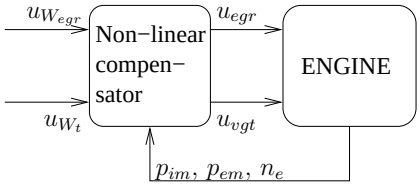

Figure 4: A block diagram of the system with a non-linear compensator on the EGR and VGT actuator. This non-linear compensator is an inversion of the models for EGR-flow and turbine flow having actuator position as input and flow as output.

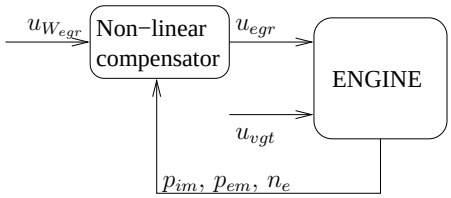

Figure 5: A block diagram of the system with a non-linear compensator on the EGR actuator. This non-linear compensator is an inversion of the EGR-flow model having actuator position as input and flow as output.

$$v_{egr} = -\frac{c_{egr2}}{2\,c_{egr1}} - \sqrt{\max\left(\left(\frac{c_{egr2}}{2\,c_{egr1}}\right)^2 - \frac{c_{egr3}}{c_{erg1}} + \frac{f_{egr}}{c_{egr1}}, 0\right)} \tag{18}$$

$$u_{egr} = \begin{cases} u_{egr}^{max} & \text{if } v_{egr} \geq u_{egr}^{max} \\ v_{egr} & \text{if } u_{egr}^{min} < v_{egr} < u_{egr}^{max} \\ u_{egr}^{min} & \text{if } v_{egr} \leq u_{egr}^{min} \end{cases} \tag{19}$$

where Ψ_{egr} is given by (9) and (10). The exhaust manifold temperature T_{em} is calculated using the model in [15] and [6]

$$T_{em} = T_{amb} + (T_e - T_{amb})\, e^{-\frac{h_{tot}\,\pi\,d_{pipe}\,l_{pipe}\,n_{pipe}}{W_{eo}\,c_{pe}}} \tag{20}$$

where

$$W_{eo} = W_{ei} + W_f, \quad T_e = T_{im} + \frac{q_{HV}\, f_{Te}(W_f, n_e)}{c_{pe}\, W_{eo}} \tag{21}$$

and

$$f_{Te}(W_f, n_e) = c_{fTe1}\, W_f + c_{fTe2}\, n_e + c_{fTe3}\, W_f\, n_e + c_{fTe4} \tag{22}$$

and $W_{ei} = W_{ei}(p_{im}, n_e)$ and $W_f = W_f(n_e, u_\delta)$. The signals p_{im}, p_{em}, and n_e are measured. Further, in the non-linear compensator it is assumed that the EGR-actuator is ideal, i.e. $\tilde{u}_{egr} = u_{egr}$.

Solving (11) for $\tilde{u}_{egr}$ results only in one solution according to (18) since f_{egr} is saturated in (11) when $\tilde{u}_{egr} > -c_{egr2}/(2\,c_{egr1})$. To avoid a complex solution

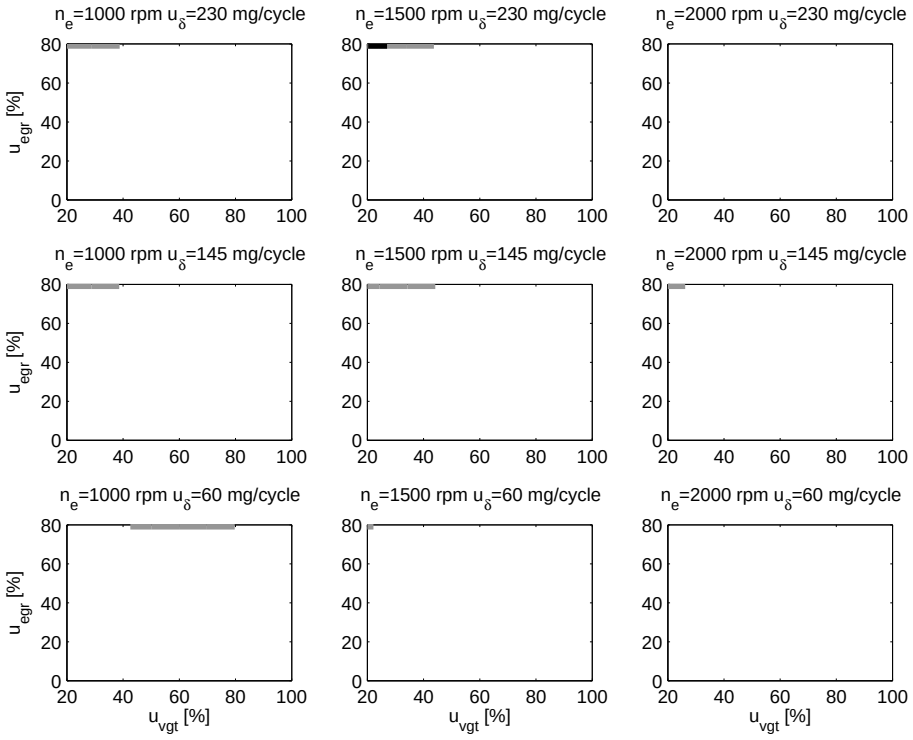

Figure 6: For the system in Fig. 5, the channel $u_{vgt} \to \lambda_O$ has a sign reversal at the gray line and $u_{vgt} \to p_{em}$ has a sign reversal at the black line. Both these sign reversals only occur when the EGR-valve is saturated.

in (18), a max-selector is used inside the square root sign. A max-selector is also used in (17) to avoid a division by zero when $\Psi_{egr} = 0$. Finally, saturation is used in (19).

The goal is now to investigate how the non-linear compensator for the EGR-actuator handles the sign reversals and the non-linear effects in $u_{vgt} \to \lambda_O$ and $u_{vgt} \to p_{em}$. This is done by simulating step responses in u_{vgt} for the system in Fig. 5. The sign reversal in $u_{vgt} \to \lambda_O$ and $u_{vgt} \to p_{em}$ are mapped in Fig. 6 in the same way as in Fig. 2 and the result is that there is no sign reversal in $u_{vgt} \to \lambda_O$ and $u_{vgt} \to p_{em}$ when $u_{egr} < 80\%$. However, when the EGR-valve is saturated at $u_{egr} = 80\%$, there are sign reversals that occur at the same operating points as in Fig. 2 where $u_{egr} = 80\%$.

Further, there are still large non-linear effects in $u_{vgt} \to \lambda_O$ and $u_{vgt} \to p_{em}$ when $u_{egr} < 80$. This is illustrated by calculating the quotient between the maximum and minimum DC-gain for the operating region in Fig. 6 when $u_{egr} < 80$. The result is that

$$\frac{\max(K_{u_{vgt} \to \lambda_O})}{\min(K_{u_{vgt} \to \lambda_O})} = 6.2 \cdot 10^3 \tag{23}$$

$$\frac{\max(K_{u_{vgt} \to p_{em}})}{\min(K_{u_{vgt} \to p_{em}})} = 1.0 \cdot 10^4 \tag{24}$$

where $K_{u_{vgt}\to\lambda_O}$ and $K_{u_{vgt}\to p_{em}}$ are the DC-gains for $u_{vgt} \to \lambda_O$ and $u_{vgt} \to p_{em}$. For linear systems, these quotients are equal to 1, and consequently there are still significant non-linear effects for the system in Fig. 5.

5.2 Inversion of position to flow model for EGR and VGT

To handle the non-linear effects in $u_{vgt} \to \lambda_O$ and $u_{vgt} \to p_{em}$ in the quotients (23) and (24), a non-linear compensator for both the EGR and VGT actuator is used according to Fig. 4. The non-linear compensator for the EGR actuator is described in the previous section and the non-linear compensator for the VGT actuator is a static inversion of the turbine flow model (12) to (14) having actuator position as input and flow as output. This inversion results in the following expression for u_{vgt} with u_{W_t} as a new control input

$$f_{vgt} = \frac{u_{W_t}\sqrt{T_{em}\, R_e}}{A_{vgtmax}\, p_{em}\, \max\left(f_{\Pi t}, 0.1\right)} \tag{25}$$

$$v_{vgt} = c_{vgt2} - c_{vgt1}\sqrt{\max\left(1 - \left(\frac{\max\left(f_{vgt} - c_{f2}, 0\right)}{c_{f1}}\right)^2, 0\right)} \tag{26}$$

$$u_{vgt} = \begin{cases} u_{vgt}^{max} & \text{if } v_{vgt} \geq u_{vgt}^{max} \\ v_{vgt} & \text{if } u_{vgt}^{min} < v_{vgt} < u_{vgt}^{max} \\ u_{vgt}^{min} & \text{if } v_{vgt} \leq u_{vgt}^{min} \end{cases} \tag{27}$$

where $f_{\Pi t}$ is given by (13) and T_{em} is given by (20)–(22). The pressure p_{em} is measured. Further, it is assumed that the VGT-actuator is ideal, i.e. $\tilde{u}_{vgt} = u_{vgt}$.

The first max-selector in (26) is used to avoid a complex solution and the second max-selector is used so that v_{vgt} is constant when $f_{vgt} < c_{f2}$. A max-selector is also used in (25) to avoid a division by zero when $f_{\Pi t} = 0$. Finally, saturation is used in (27).

Simulations show that the system in Fig. 5 is stable and that the system in Fig. 4 is unstable. The unstable system in Fig. 4 is stabilized by a controller in Sec. 6. The physical explanation of this instability is as follows. A positive step in u_{W_t} according to Fig. 7 leads to an increase in u_{vgt} and therefore a decrease in p_{em}. Since the output u_{vgt} from the non-linear compensator increases when p_{em} decreases, the non-linear compensator will continue to open up the VGT until it is saturated, and the result is an error between u_{W_t} and the turbine mass flow W_t. This instability is further analyzed in Sec. 5.3 by investigating stability of linearized models of the system in Fig. 4.

To investigate the system in Fig. 4 for non-linear effects in $u_{vgt} \to \lambda_O$ and $u_{vgt} \to p_{em}$, the quotients

$$\frac{\max(K_{u_{W_t}\to\lambda_O})}{\min(K_{u_{W_t}\to\lambda_O})}, \quad \frac{\max(K_{u_{W_t}\to p_{em}})}{\min(K_{u_{W_t}\to p_{em}})}$$

are calculated for the operating region in Fig. 6 when $u_{egr} < 80$. $K_{u_{W_t}\to\lambda_O}$ and $K_{u_{W_t}\to p_{em}}$ are the DC-gains for $u_{W_t} \to \lambda_O$ and $u_{W_t} \to p_{em}$ between different

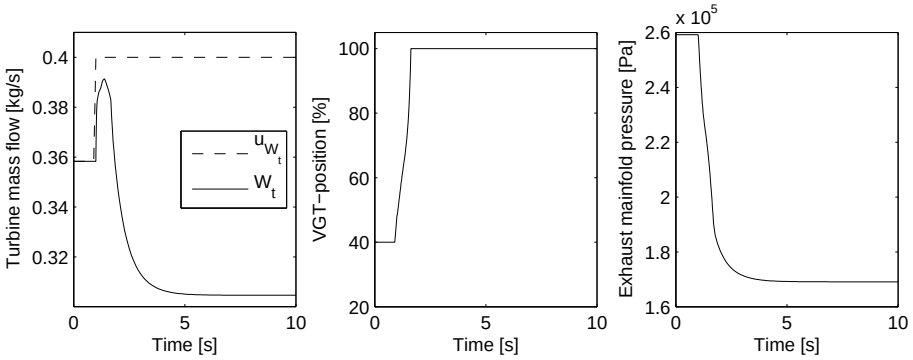

Figure 7: A step response of the system in Fig. 4 with $u_{W_{egr}} = 0.04$ kg/s showing that this system is unstable.

stationary points. However, these DC-gains can not be calculated directly since the stationary points are unstable for the system in Fig. 4. Therefore, these DC-gains are calculated using the chain rule according to

$$K_{u_{W_t} \to \lambda_O} = \frac{K_{u_{vgt} \to \lambda_O}}{K_{u_{vgt} \to W_t}} \tag{28}$$

$$K_{u_{W_t} \to p_{em}} = \frac{K_{u_{vgt} \to p_{em}}}{K_{u_{vgt} \to W_t}} \tag{29}$$

where the DC-gains $K_{u_{vgt} \to \lambda_O}$, $K_{u_{vgt} \to p_{em}}$, and $K_{u_{vgt} \to W_t}$ are calculated from step responses in u_{vgt} for the system in Fig. 5. The result is that

$$\frac{\max(K_{u_{W_t} \to \lambda_O})}{\min(K_{u_{W_t} \to \lambda_O})} = 77 \tag{30}$$

$$\frac{\max(K_{u_{W_t} \to p_{em}})}{\min(K_{u_{W_t} \to p_{em}})} = 30 \tag{31}$$

Comparing these quotients with (23) and (24), the conclusion is that the system in Fig. 4 has less non-linear effects compared to the system in Fig. 5.

5.3 Stability analysis of the open-loop system

A mapping of poles for linearized models of the system in Fig. 4 is performed in order to analyze the stability of these models. The linear models are constructed by linearizing the non-linear system in Fig. 4 where the block "ENGINE" is the eight-order model in Sec. 2. The linearization is performed in the same operating points as the operating points in Fig. 2 and 6. The linear models have the form

$$\begin{aligned} \dot{x} &= A_i\, x + B_i\, u \\ y &= C_i\, x + D_i\, u \end{aligned} \tag{32}$$

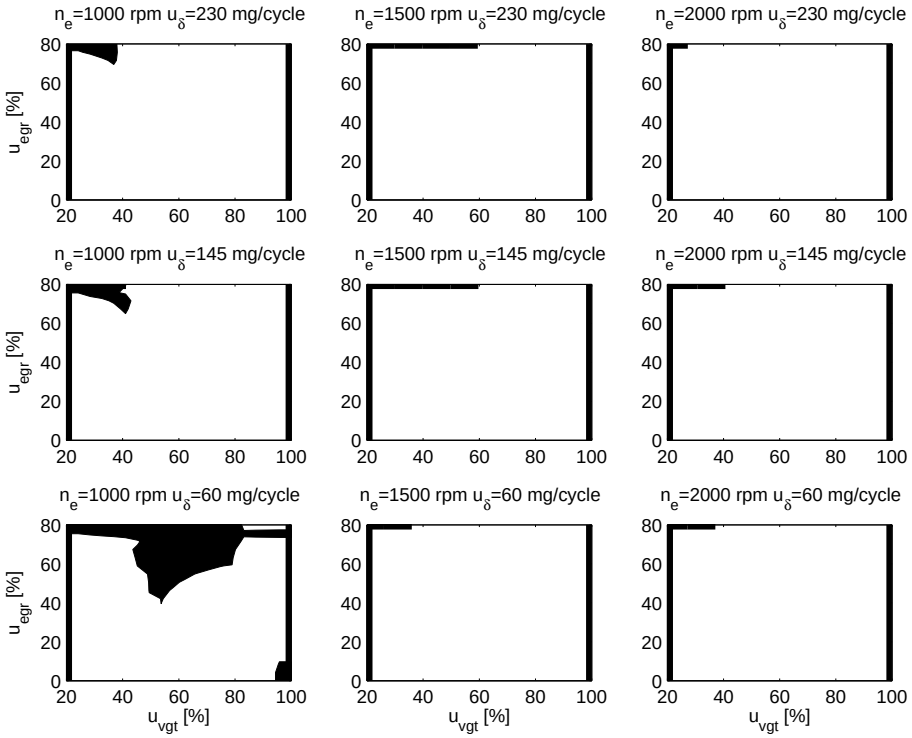

Figure 8: A mapping of poles for linearized models of the system in Fig. 4 showing that there is one pole in the right complex half plane for almost the complete operating region except in the black areas and at the thick black lines where all poles are in the left complex half plane. In the thin white area in the upper right corner in the left bottom plot, u_{egr} is equal to 80%.

where i is the operating point number and

$$
\begin{aligned}
u &= [u_{W_{egr}} \quad u_{W_t}]^T \\
x &= [p_{im} \quad p_{em} \quad X_{Oim} \quad X_{Oem} \quad \omega_t \quad \tilde{u}_{egr1} \quad \tilde{u}_{egr2} \quad \tilde{u}_{vgt}]^T \\
y &= [W_{egr} \quad p_{em}]^T
\end{aligned}
$$

The motives for selecting W_{egr} and p_{em} as outputs will be described in Sec. 6.1.

A mapping of the poles for the models (32) are performed in Fig. 8 showing that there is one pole in the right complex half plane for almost the complete operating region except in the black areas and at the thick black lines where all poles are in the left complex half plane. Consequently, the linearized models (32) are stable only in the black areas and at the thick black lines in Fig. 8.

6 Control structure with non-linear compensator

The control design objective is to coordinate $u_{W_{egr}}$ and u_{W_t} in Fig. 4 in order to achieve the control objectives stated in Sec. 1.1. The approach is to build a controller structure using min/max-selectors and PID controllers similar to the

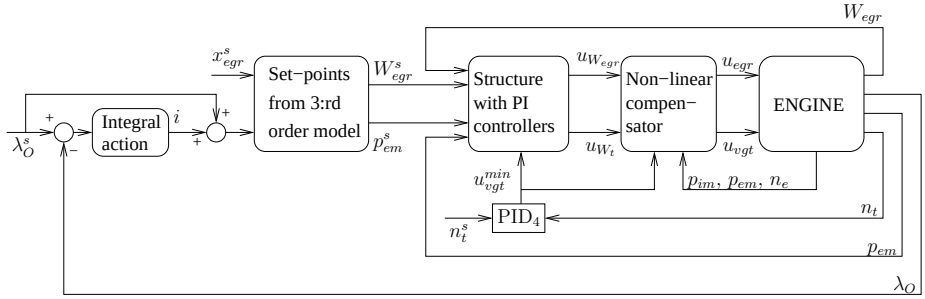

Figure 9: Block diagram of the closed-loop system, showing; an integral action on λ_O, set-points calculations, a structure with PI controllers, a PID controller for the turbocharger speed n_t, and a non-linear compensator.

structure (15) and (16). The solution is presented step by step in the following sections and a block diagram of the proposed closed-loop system is shown in Fig. 9.

6.1 Main feedback loops

The first step in the control design is to choose outputs and main feedback loops. It is natural to choose the EGR flow W_{egr} and the turbine flow W_t as outputs due to that $u_{W_{egr}} = W_{egr}$ and $u_{W_t} = W_t$ if there are no model errors in the non-linear compensator. However, the system can not be stabilized using these outputs. The reference [5] shows that if W_{egr} and the compressor flow W_c are chosen as outputs in feedback linearization, there will be an unstable zero dynamics in p_{em}. To handle this unstable mode, W_{egr} and p_{em} are chosen as outputs. Therefore, the following main feedback loops are chosen

$$u_{W_{egr}} = \mathrm{PI}_1(W^s_{egr}, W_{egr}) \tag{33}$$

$$u_{W_t} = -\mathrm{PI}_2(p^s_{em}, p_{em}) \tag{34}$$

These two main feedback loops are selected to handle items 1 and 3 of the control objectives stated in Sec. 1.1 where the set-points λ^s_O and x^s_{egr} are transformed to the set-points W^s_{egr} and p^s_{em} according to the following section.

6.2 Set-point transformation and integral action

The set-points λ^s_O and x^s_{egr} are transformed to the set-points W^s_{egr} and p^s_{em} in two steps. Firstly, the equilibriums for W_c and W_{egr} of the mass balances (1b)–(1d) are calculated from λ^s_O and x^s_{egr}

$$W^s_c = \frac{W_f}{2\,X_{Oc}}\left(\beta + \sqrt{\beta^2 + 4\,\lambda^s_O\,(O/F)_s(1 - x^s_{egr})X_{Oc}}\right) \tag{35}$$

$$W^s_{egr} = \frac{x^s_{egr}}{1 - x^s_{egr}} W_c \tag{36}$$

where

$$\beta = (\lambda^s_O\,(O/F)_s - X_{Oc})(1 - x^s_{egr}) + (O/F)_s\,x^s_{egr},$$

X_{Oc} is the constant oxygen concentration in air passing the compressor, and $(O/F)_s$ is the stoichiometric relation between oxygen and fuel masses. Note that W_c is used instead of W_c^s in (36) in order to get the correct value of W_{egr}^s in stationary points when $W_c > W_c^s$, i.e. when $\lambda_O > \lambda_O^s$ that is allowed in diesel engines. Secondly, the equilibriums for p_{im} and p_{em} of a third-order model are calculated from W_c^s and x_{egr}^s. This third-order model is a simplification of the eighth-order model in Sec. 2 and the three states in the simplified model are p_{im}, p_{em}, and the compressor power P_c. This model is based on the control design model developed in [5]:

$$\begin{aligned} \dot{p}_{im} &= k_{im}\,(W_c + u_1 - k_e\,p_{im}) \\ \dot{p}_{em} &= k_{em}\,(k_e\,p_{im} - u_1 - u_2 + W_f) \\ \dot{P}_c &= \frac{1}{\tau}(\eta_m\,P_t - P_c) \end{aligned} \tag{37}$$

$$\begin{aligned} W_c &= \frac{\eta_c\,P_c}{T_{amb}\,c_{pa}\,((p_{im}/p_{amb})^{\mu_a} - 1)} \\ P_t &= \eta_t\,c_{pe}\,T_{em}\,(1 - (p_{amb}/p_{em})^{\mu_e})\;u_2 \end{aligned}$$

The variables $k_{em} = k_{em}(T_{em})$, $W_f = W_f(u_\delta, n_e)$, $k_e = k_e(n_e)$, and η_c are treated as external slowly varying signals and k_{im}, τ, η_m, T_{amb}, c_{pa}, p_{amb}, μ_a, η_t, c_{pe}, and μ_e are constants.

The equilibriums for p_{im} and p_{em} of the third-order model (37) are

$$\begin{aligned} p_{im}^s &= \frac{W_c^s}{k_e(1 - x_{egr}^s)} \\ p_{em}^s &= p_{amb}\left(1 - \frac{c_{pa}\left(\left(\frac{p_{im}^s}{p_{amb}}\right)^{\mu_a} - 1\right)T_{amb}\,W_c^s}{c_{pe}\,\eta_{cmt}\,T_{em}^s(W_c^s + W_f)}\right)^{-\frac{1}{\mu_e}} \end{aligned} \tag{38}$$

where $\eta_{cmt} = \eta_c^s\,\eta_m\,\eta_t$. The set-point T_{em}^s for the exhaust manifold temperature is calculated using the model in [15] and [6]

$$T_{em}^s = T_{amb} + (T_e - T_{amb})\,e^{-\frac{h_{tot}\,\pi\,d_{pipe}\,l_{pipe}\,n_{pipe}}{W_{eo}^s\,c_{pe}}}$$

where

$$W_{eo}^s = \frac{W_c^s}{1 - x_{egr}^s} + W_f, \quad T_e = T_{im} + \frac{q_{HV}\,f_{Te}(W_f, n_e)}{c_{pe}\,W_{eo}^s}$$

and

$$f_{Te}(W_f, n_e) = c_{fTe1}\,W_f + c_{fTe2}\,n_e + c_{fTe3}\,W_f\,n_e + c_{fTe4}$$

The set-point η_c^s for the compressor efficiency is calculated using the model in [15]

$$\eta_c^s = \eta_{cmax} - \chi^T\,Q_c\,\chi$$

χ is a vector which contains the inputs

$$\chi = \begin{bmatrix} W_c^s - W_{copt} \\ \pi_c - \pi_{copt} \end{bmatrix}$$

where the non-linear transformation for $\frac{p^s_{im}}{p_{amb}}$ is

$$\pi_c = \left(\frac{p^s_{im}}{p_{amb}} - 1 \right)^{c_\pi}$$

and the symmetric and positive definite matrix Q_c consists of three parameters

$$Q_c = \begin{bmatrix} a_1 & a_3 \\ a_3 & a_2 \end{bmatrix}$$

The model parameters η_{cmax}, a_1, a_2, and a_3 are tuned according to [15].

Integral action

If the control structure is applied on a higher order model or a real engine, there will be control errors for λ_O. This is due to that the equilibriums (38) for the third order model are not the same as the equilibriums for p_{im} and p_{em} of a higher order model or a real engine due to model errors in the third order model. In order to decrease these control errors, the following integral action is used

$$\frac{di}{dt} = K_{\lambda_O} \, e_{\lambda_O} \tag{39}$$

where $e_{\lambda_O} = \lambda^s_O - \lambda_O$. The state i is fed into W^s_c in (35) according to

$$\begin{aligned} W^s_c =& \frac{W_f}{2\, X_{Oc}} \cdot \\ & \left(\beta + \sqrt{\beta^2 + 4\,(\lambda^s_O + i)(O/F)_s (1 - x^s_{egr}) X_{Oc}} \right) \\ \beta =& ((\lambda^s_O + i)(O/F)_s - X_{Oc})(1 - x^s_{egr}) + (O/F)_s \, x^s_{egr} \end{aligned}$$

The set-point transformation (36) between x^s_{egr} and W^s_{egr} is based on the definition of x_{egr} in (7) and does not have any model errors and consequently there is no need of using integral action on x_{egr}.

6.3 Saturation levels

The saturation levels for the control inputs $u_{W_{egr}}$ and u_{W_t} are calculated using the models for the EGR-flow (8) and the turbine flow (12) in the following way. The saturation levels for $u_{W_{egr}}$ are calculated as

$$W^{min}_{egr} = \frac{A_{egrmax} \, f_{egr}(u^{min}_{egr}) \, p_{em} \, \max(\Psi_{egr}, 0.1)}{\sqrt{T_{em} \, R_e}} \tag{40}$$

$$W^{max}_{egr} = \frac{A_{egrmax} \, f_{egr}(u^{max}_{egr}) \, p_{em} \, \max(\Psi_{egr}, 0.1)}{\sqrt{T_{em} \, R_e}} \tag{41}$$

where $f_{egr}(u^{min}_{egr})$ and $f_{egr}(u^{max}_{egr})$ are given by (11), and u^{min}_{egr} and u^{max}_{egr} are the saturations levels for u_{egr}. The saturation levels for u_{W_t} are calculated as

$$W^{min}_t = \frac{A_{vgtmax} \, p_{em} \, \max\left(f_{\Pi t}, 0.1\right) \, f_{vgt}(u^{min}_{vgt})}{\sqrt{T_{em} \, R_e}} \tag{42}$$

$$W_t^{max} = \frac{A_{vgtmax}\, p_{em}\ \max\left(f_{\Pi t}, 0.1\right)\ f_{vgt}(u_{vgt}^{max})}{\sqrt{T_{em}\, R_e}} \tag{43}$$

where $f_{vgt}(u_{vgt}^{min})$ and $f_{vgt}(u_{vgt}^{max})$ are given by (14), and u_{vgt}^{min} and u_{vgt}^{max} are the saturations levels for u_{vgt}. To get the correct values on the saturation levels (40)–(43), the max-selectors in (17) and (25) have to be used in the same way in (40)–(43).

6.4 Additional control modes

In order to achieve the control objectives 3, 5, and 6 stated in Sec. 1.1, additional control modes are added to the main control loops (33)–(34) according to

$$u_{W_{egr}}(t_i) = \begin{cases} W_{egr}^{max} & \text{, if } (u_{W_{egr}}(t_{i-1}) = W_{egr}^{max})\& \\ & \quad (e_{W_{egr}} > -5 \cdot 10^{-3}) \\ \mathrm{PI}_1(W_{egr}^s, W_{egr}) & \text{, else} \end{cases} \tag{44}$$

$$u_{W_t}(t_i) = \begin{cases} \min(-\mathrm{PI}_2(p_{em}^s, p_{em}), \\ -\mathrm{PI}_3(W_{egr}^s, W_{egr})) & \text{, if } u_{W_{egr}}(t_{i-1}) = W_{egr}^{max} \\ -\mathrm{PI}_2(p_{em}^s, p_{em}) & \text{, else} \end{cases} \tag{45}$$

$$u_{vgt}^{min} = -\mathrm{PID}_4(e_{nt}) \tag{46}$$

where $e_{W_{egr}} = W_{egr}^s - W_{egr}$ and $e_{nt} = n_t^s - n_t$. The additional control modes in the structure (44)–(46) are motivated as follows. In operating points with low engine torque there is too little EGR-flow although $u_{W_{egr}}$ is saturated at W_{egr}^{max}. To achieve control objective 3 also for these operating points, a higher EGR-flow is obtainable by decreasing u_{W_t} when $u_{W_{egr}} = W_{egr}^{max}$ using $\mathrm{PI}_3(W_{egr}^s, W_{egr})$ in (45). The appropriate value for u_{W_t} is then the smallest value of the outputs from the two different PI controllers. To achieve control objective 5 and avoid over-speeding of the turbo, the lower saturation level u_{vgt}^{min} for the VGT is influenced by the turbine speed n_t in (46). In this case n_t is controlled with u_{vgt}^{min} to a set-point n_t^s which has a value slightly lower than the maximum limit n_t^{max} in order to avoid that overshoots shall exceed n_t^{max}. This means that u_{vgt}^{min} will open up the VGT, thereby decreasing the input torque to the turbocharger, and thereby keeping its speed within limits. The PID controller in (46) benefits from a derivative parts in order to predict high turbocharger speeds [13]. The other saturation levels for u_{egr} and u_{vgt} are set to $u_{egr}^{min} = 0$, $u_{egr}^{max} = 80$, and $u_{vgt}^{max} = 100$. The saturation levels for PID_4 are set to 22 and 100.

Further, the proposed control structure (44)–(46) gives priority to x_{egr} before λ_O or equivalent it gives priority to W_{egr} before p_{em} during aggressive load transients. This can be seen in the following way. During aggressive load transients, p_{em}^s increases yielding a decrease in u_{W_t}. If p_{em}^s is too large, u_{W_t} is saturated at W_t^{min} and p_{em}^s is not reached while $u_{W_{egr}}$ controls W_{egr}. Consequently, W_{egr} has higher priority than p_{em}.

Pumping minimization and handling of other control objectives

This structure also minimizes the pumping work in stationary points by striving to open the actuators as much as possible. Consequently, control objective 6 is

achieved, and this can be understood as follows. The important controller action is coupled to λ_O and p_{em}, and in particular the operating conditions where there is a degree of freedom when $\lambda_O > \lambda_O^s$. For these conditions $p_{em} > p_{em}^s$ since p_{em} and p_{em}^s increases when λ_O and λ_O^s increases for constant x_{egr}. There are two cases to consider for these conditions. In the first case the proposed controller strives to reduce p_{em} by opening the VGT, through the second row in (45). To maintain W_{egr}^s, the second row in (44) forces the EGR-valve to be opened as much as possible. Either p_{em}^s is reached or $\mathrm{PI}_2(p_{em}^s, p_{em})$ saturates at W_t^{max}, due to the integral action. In the other case, coupled to the first rows in (44)–(45), the EGR-valve is fully open and it is necessary to increase W_{egr} by closing the VGT to reach W_{egr}^s. In both cases the actuators are thus opened as much as possible while achieving control objectives 1 and 3 and this minimizes the pumping work according to [13].

In case 1 in (44) $u_{W_{egr}}$ is locked to W_{egr}^{max} until $e_{W_{egr}} > -5 \cdot 10^{-3}$ in order to avoid undesirable oscillations between case 1 and 2 in (45). Further, control objective 2 and 4 are achieved using feedforward fuel control and a smoke limiter in the same way as in [13].

6.5 Integral action with anti-windup

The integral action (39) is implemented in discrete form with anti-windup according to Algorithm 1 that is motivated as follows. In operating points where u_{W_t} or $u_{W_{egr}}$ are saturated at their maximum values and $e_{p_{em}} < 0$, p_{em} can not be decreased to get $e_{p_{em}} = 0$ while controlling W_{egr}. Consequently, λ_O can not be decreased to get $e_{\lambda_O} = 0$ leading to that $e_{\lambda_O} < 0$ and $i \to -\infty$. To handle this and affect i so that $i \to 0$ for these operating points, row 2 in Algorithm 1 is executed that is a discrete form of $di/dt = -\delta\, i$ if $\alpha_1 = i_n$. In order to increase i if $e_{\lambda_O} > 0$, a max-selector between α_1 and α_2 is used in row 4, where $\alpha_2 := i_{n-1} + T_s\, K_{\lambda_O}\, e_{\lambda_O}$ in row 3 is a discrete form of (39) if $\alpha_2 = i_n$. Further, due to noise, time delays, and dynamics in the system there are some few operating points where $e_{\lambda_O} \ll 0$, $u_{vgt} \ll 100$, and $u_{egr} < 80$ leading to that $i \to -\infty$ slowly. To handle this, row 2–4 are also executed when $e_{\lambda_O} < -1$ and $u_{vgt} > 50$, otherwise row 6 is executed. Moreover, in operating points where $u_{W_t} = W_t^{min}$ or $p_{em}^s > 10^6$, p_{em} can not reach p_{em}^s leading to that $e_{p_{em}} > 0$ while controlling W_{egr}. This leads to that λ_O can not reach λ_O^s leading to that $e_{\lambda_O} > 0$ and $i \to +\infty$. To handle this and limit i for these operating points, a min-selector between α_3 and i_{n-1} is used in row 9, otherwise row 11 is executed.

6.6 PID parameterization and implementation

Each PI controller in (44)–(45) has the following parameterization

$$\mathrm{PI}_j(y^s, y) = K_j \left(\alpha_j\, y^s - y + \frac{1}{T_{ij}} \int (y^s - y)\, dt \right) \tag{47}$$

where the index j is the number of the different PI controllers. The PID controller in (46) has the following parameterization

$$\mathrm{PID}_4(e) = K_4 \left(e + \frac{1}{T_{i4}} \int e\, dt + T_{d4} \frac{de}{dt} \right) \tag{48}$$

Algorithm 1 Integral action with anti-windup

if ($e_{p_{em}} < 0$ **and** ($u_{W_t} = W_t^{max}$ **or** $u_{W_{egr}} = W_{egr}^{max}$)) **or**
($e_{\lambda_O} < -1$ **and** $u_{vgt} > 50$) **then**
  $\alpha_1 := i_{n-1} - T_s\,\delta\,i_{n-1}$
  $\alpha_2 := i_{n-1} + T_s\,K_{\lambda_O}\,e_{\lambda_O}$
  $\alpha_3 := \max(\alpha_1, \alpha_2)$
else
  $\alpha_3 := i_{n-1} + T_s\,K_{\lambda_O}\,e_{\lambda_O}$
end if
if $u_{W_t} = W_t^{min}$ **or** $p_{em}^s > 10^6$ **then**
  $i_n := \min(\alpha_3, i_{n-1})$
else
  $i_n := \alpha_3$
end if

that does not benefit from the tuning parameter α_j in (47) due to that the set-point n_t^s in (46) is constant. The PI and PID controllers are implemented in incremental form which leads to anti-windup and bump-less transfer between the different control modes [17].

6.7 Stability analysis of the closed-loop system

To analyze if the proposed control structure (44)–(45) stabilizes the linearized models (32), the control structure is applied to these linearized models and the closed-loop poles are mapped. The control parameters are tuned using the method in [14] with $\gamma_{Me} = 3/2$ and $\gamma_{egr} = 1$. Each control mode in (44)–(45) is analyzed separately resulting in linear closed-loop systems. The poles for these closed-loop systems are mapped in Fig. 10 showing that all poles are in the left complex half plane for almost the complete operating region except in operating points at the thick black line in the left bottom plot where there is one pole in the right complex half plane. Further, the system analysis in [16] shows that the DC-gain from u_{vgt} to x_{egr} has reversed sign (positive sign) in these unstable operating points. The question is what effect this instability and sign reversal have on the control performance. Simulations show that if the system operates in these unstable points in the beginning of a transient and $W_{egr} < W_{egr}^s$, the VGT position decreases until $W_{egr} = W_{egr}^s$ (according to $\mathrm{PI}_3(W_{egr}^s, W_{egr})$) in (45)). Consequently the system will leave the unstable operating points. If the system operates in the unstable points in the beginning of a transient and $W_{egr} > W_{egr}^s$, the VGT position increases until it is fully open, and then $\mathrm{PI}_1(W_{egr}^s, W_{egr})$ in (44) becomes active and closes the EGR-valve until $W_{egr} = W_{egr}^s$. Consequently, the system can not get caught in the unstable region. However, the effect of this instability and sign reversal is that there exist two sets of solutions for the EGR-valve and the VGT-position for the same value of W_{egr}^s depending on if $W_{egr} < W_{egr}^s$ or if $W_{egr} > W_{egr}^s$ in the beginning of a transient. However, the proposed control structure is not extended to handle this, since the maximum profit in pumping work would only be 2.5 mBar, which is an insignificant value.

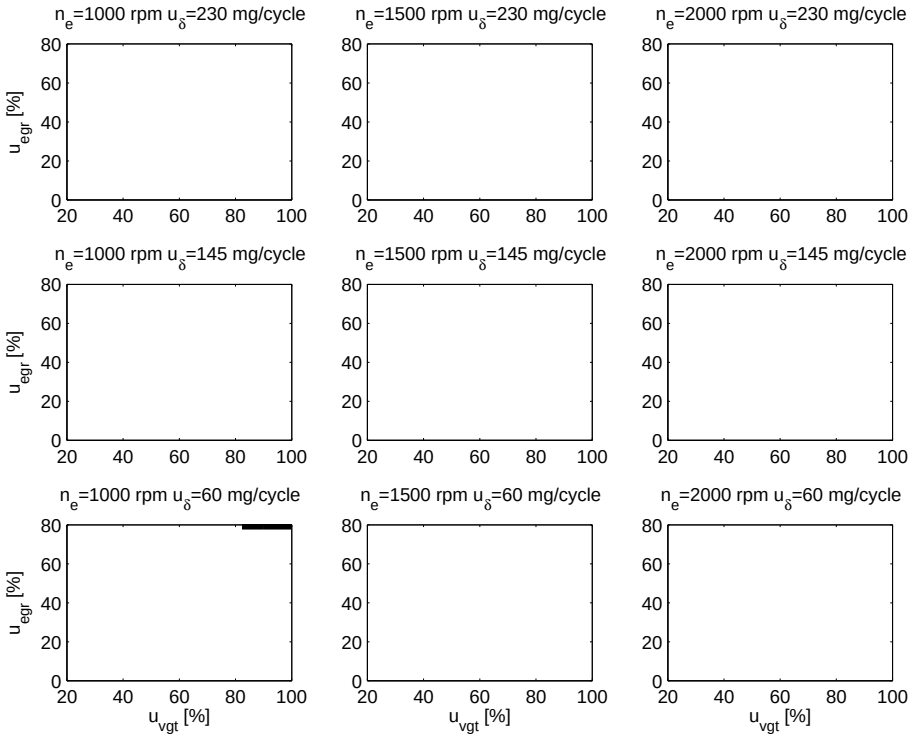

Figure 10: A mapping of poles for the closed-loop system where the proposed control structure (44)–(45) is applied to the linearized models (32). All poles are in the left complex half plane for almost the complete operating region except in operating points at the thick black line in the left bottom plot where there is one pole in the right complex half plane.

7 Engine test cell experiments

The control structure proposed in Sec. 6 is applied and validated in an engine test cell. The goal is to compare the following two control structures for the steps in Fig. 3, for an aggressive transient from the European Transient Cycle (ETC), and for the complete ETC cycle.

PID: The control structure without non-linear compensator (15)–(16).

NLC: The proposed control structure with non-linear compensator as depicted in Fig. 9.

The observer, measured signals, and tuning for PID are explained in Sec. 4. For NLC, the same observer as the one in Sec. 4.1 is used to estimate the oxygen mass fraction X_{Oim}. Once X_{Oim} is estimated, the mass flow into the engine W_{ei}, λ_O and W_{egr} are calculated using the model in Sec. 2. The engine speed (n_e), intake and exhaust manifold pressure (p_{im}, p_{em}), compressor mass flow (W_c), and turbocharger speed (n_t) are measured with production sensors. Due to measurement noise, all measured and observed variables are filtered using low pass filters with a time constant of 0.1 s. The controller parameters are initially

tuned using the method in [14] with manual initialization and $\gamma_{Me} = 3/2$ and $\gamma_{egr} = 1$, and are then manually fine tuned in the engine test cell experiments.

7.1 Comparing step responses in oxygen/fuel ratio

PID and NLC are compared in Fig. 11 for the same three steps as in Fig. 3. The result is that NLC gives approximately the same step response in λ_O for all three steps with fast control and less oscillations compared to PID. Consequently, NLC handles nonlinear effects. Further, the internal variables for NLC for this experiment in Fig. 12 show that p_{em} and W_{egr} follow their set-points and that $i_n \neq 0$ in stationary points, i.e. integral action is necessary to handle model errors in the set-point transformation.

7.2 Comparison on an aggressive ETC transient

PID and NLC are compared in Fig. 13–14 on an aggressive ETC transient showing that NLC gives less EGR-error but more λ_O-error when $\lambda_O < \lambda_O^s$. This can be understood as follows. At t=122-124 s, PID closes the VGT in order to increase x_{egr} and it closes the EGR-valve to fully closed in order to increase λ_O, yielding $x_{egr} = 0$ and a high EGR-error. However, NLC closes the VGT in order to increase p_{em} and it opens the EGR-valve in order to increase W_{egr}, yielding less EGR-error compared to PID. However, since PID closes the VGT and the EGR-valve more than NLC, PID gives a faster increase in turbocharger speed and therefore a faster increase in λ_O and less torque deficiency.

Further, at t=127-132 s x_{egr}^s is equal to zero and NLC closes the EGR-valve directly yielding $x_{egr} = 0$. However, PID has to first fully open the VGT, and then the PID can switch control mode and close the EGR-valve. This leads to a later closing of the EGR-valve and more EGR-error compared to NLC. However, since the EGR-valve is more open for PID, PID gives less pumping losses at t=126-131 s.

The differences in EGR-error, λ_O-error, and pumping losses between the two controllers at t=122-125 s are only due to that the tuning of the controllers have different trade-offs between EGR-error and λ_O-error. However, the differences in EGR-error and pumping losses at t=127-132 s are due to the selected control loops and modes in the control structures according to the explanation above. Consequently, the main benefit with NLC is that it reduces the EGR-error at t=127-132 s. However, one drawback with NLC is that it increases the pumping losses at t=126-131 s.

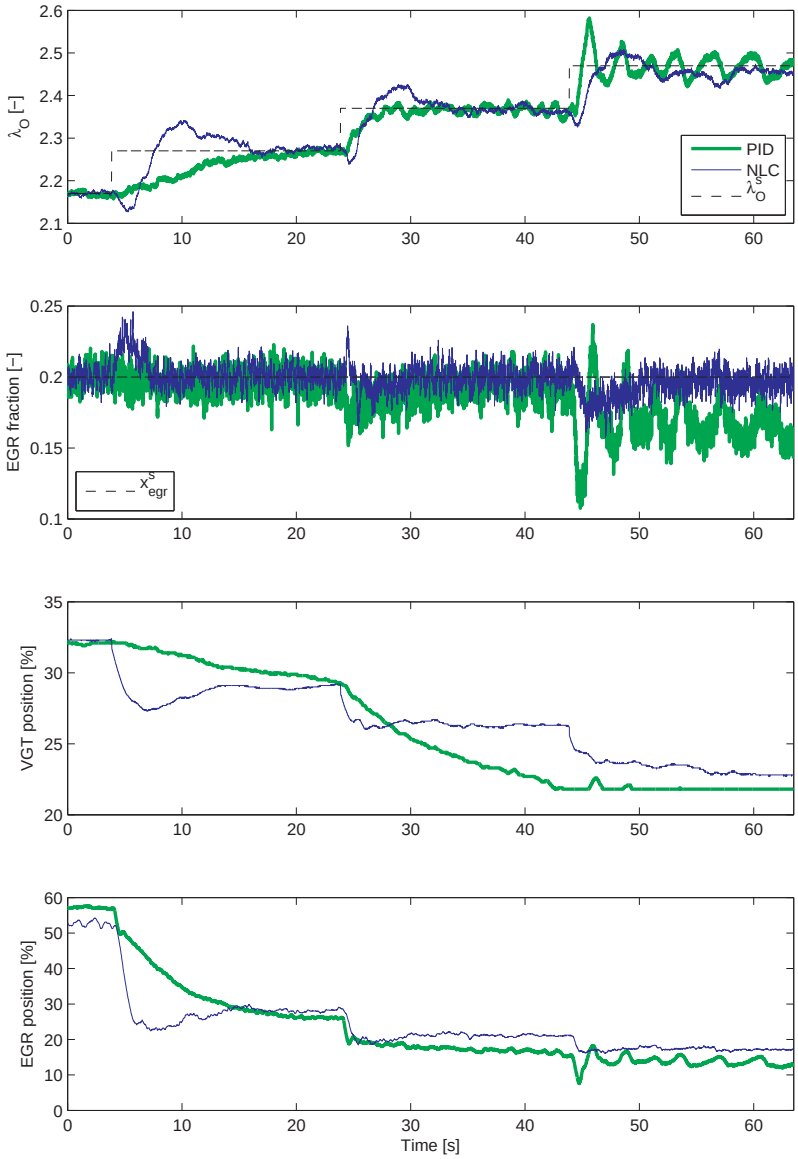

Figure 11: Comparison between PID and NLC for the same steps in λ_O^s as in Fig. 3. NLC gives approximately the same step response in λ_O for all three steps with fast control and less oscillations compared to PID. Consequently, NLC handles nonlinear effects.

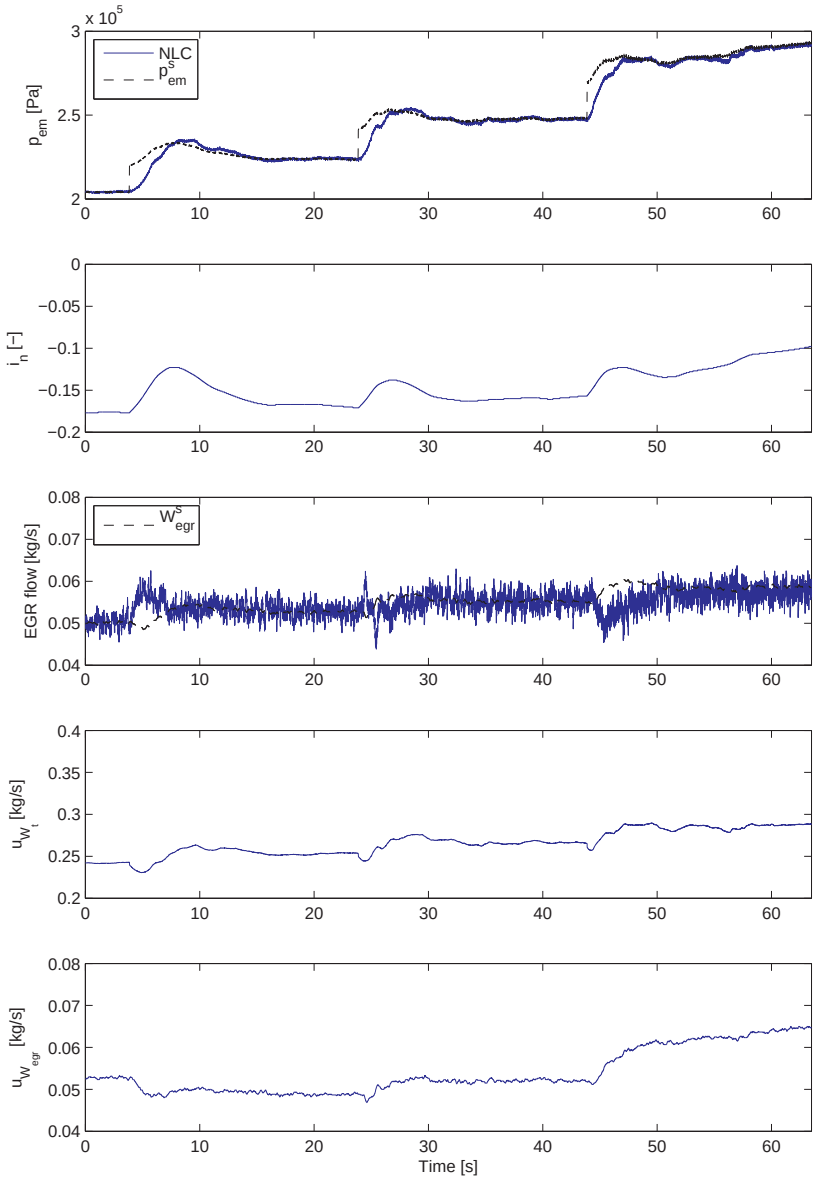

Figure 12: Validation of the internal variables for NLC for the experiment in Fig. 11 showing that p_{em} and W_{egr} follow their set-points and that $i_n \neq 0$ in stationary points, i.e. integral action is necessary to handle model errors in the set-point transformation.

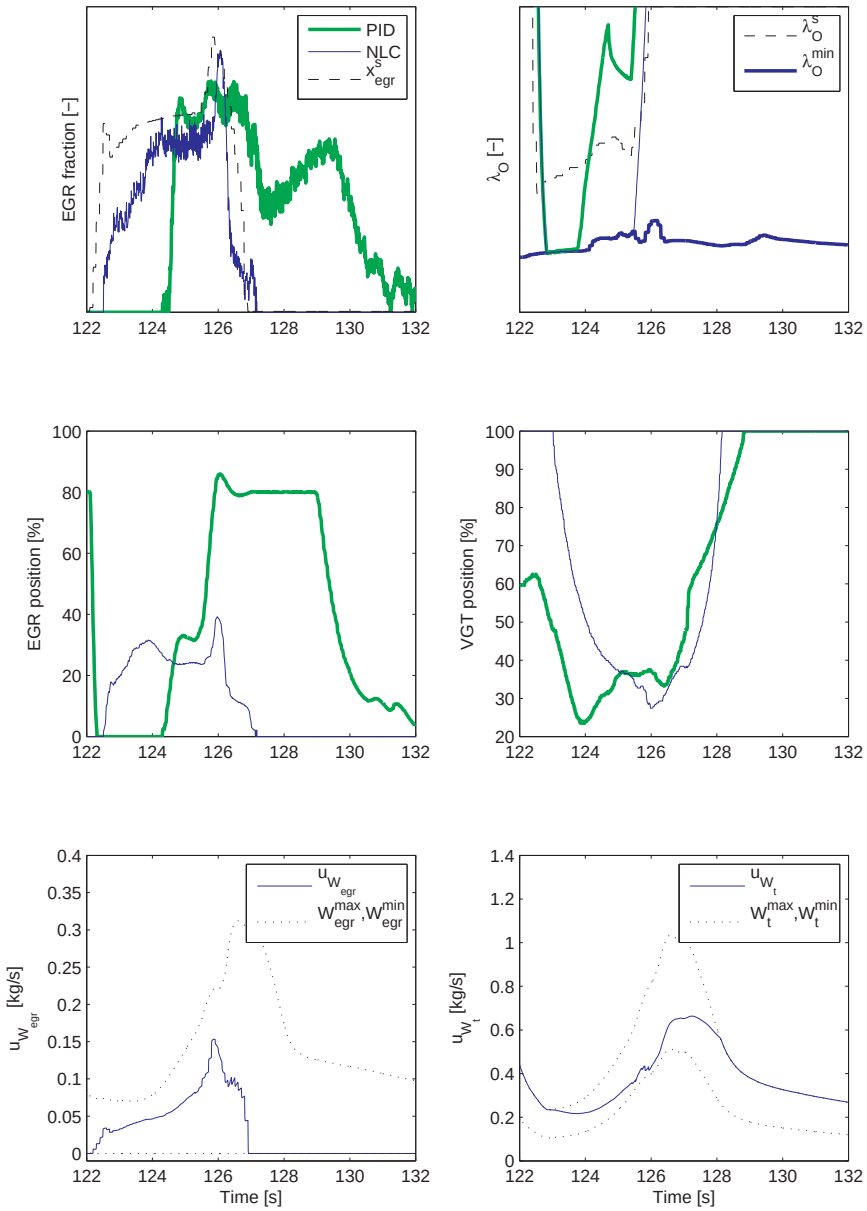

Figure 13: Comparison between PID and NLC on an aggressive ETC transient. NLC gives less EGR-error but more λ_O-error when $\lambda_O < \lambda^s_O$ compared to PID.

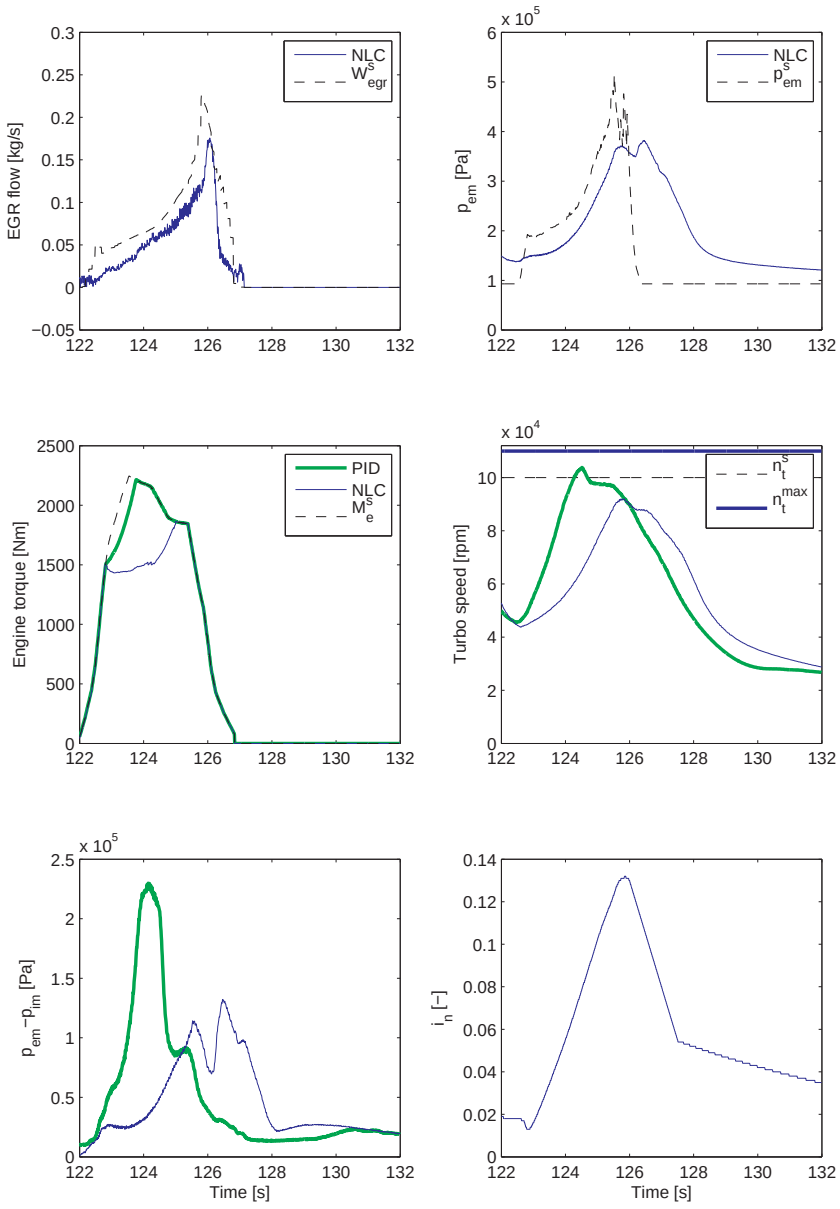

Figure 14: Comparison between PID and NLC on an aggressive ETC transient. PID gives less torque deficiency and a faster increase in turbo speed compared to NLC.

7.3 Comparison on the complete ETC cycle

PID and NLC are compared on the complete ETC cycle by comparing λ_O-error, x_{egr}-error, and pumping losses

$$\begin{aligned} E_{\lambda_O} &= \sum_{i=1}^{N} \max(e_{\lambda_O}(t_i), 0) \\ E_{x_{egr}} &= \sum_{i=1}^{N} |e_{xegr}(t_i)| \\ PMEP &= \sum_{i=1}^{N} (p_{em}(t_i) - p_{im}(t_i)) \end{aligned} \tag{49}$$

where t_i is the time at sample number i. The comparison in Tab. 1 shows that PID has 47% higher EGR-error and 13% lower pumping losses. These two differences are due to the selected control loops and modes in the control structures and that the tuning of the controllers have different trade-offs between EGR-error and λ_O-error as explained in Sec. 7.2. However, the difference in λ_O-error is only due to that the tuning of the controllers have different trade-offs.

Table 1: The measures (49) for two different controllers over the ETC cycle. The measures are normalized with respect to NLC.

Controller	E_{λ_O}	$E_{x_{egr}}$	$PMEP$
NLC	1.00	1.00	1.00
PID	0.44	1.47	0.87

8 Conclusions

Inspired by an approach in [5], a non-linear compensator has been investigated for handling of non-linear effects in diesel engines. This non-linear compensator is a non-linear state dependent input transformation that was developed by inverting the models for EGR-flow and turbine flow having actuator position as input and flow as output. This leads to two new control inputs: the EGR-flow and turbine flow. A mapping of the sign reversals in $u_{vgt} \rightarrow \lambda_O$ and $u_{vgt} \rightarrow p_{em}$ when the non-linear compensator for the EGR-actuator is used shows that they only occur when the EGR-valve is saturated. Further, a stability analysis of linearized models of the open-loop system with a non-linear compensator shows that these models are unstable in a large operating region. This system is stabilized by a control structure that consists of PID controllers and min/max-selectors. The EGR flow and the exhaust manifold pressure are chosen as feedback variables in this structure. Further, the set-points for λ_O and x_{egr} are transformed to set-points for the feedback variables. In order to handle model errors in this set-point transformation, an integral action on λ_O is used in an outer loop. Experimental validations of the proposed control structure show that it handles nonlinear effects, and that it reduces EGR-errors but increases the pumping losses compared to a control structure without non-linear compensator.

References

[1] M. Ammann, N.P. Fekete, L. Guzzella, and A.H. Glattfelder. Model-based Control of the VGT and EGR in a Turbocharged Common-Rail Diesel Engine: Theory and Passenger Car Implementation. *SAE Technical paper 2003-01-0357*, January 2003.

[2] A. Amstutz and L. Del Re. EGO sensor based robust output control of EGR in diesel engines. *IEEE Transactions on Control System Technology*, pages 37–48, 1995.

[3] L. Guzzella and A. Amstutz. Control of diesel engines. *IEEE Control Systems Magazine*, 18:53–71, 1998.

[4] J.B. Heywood. *Internal Combustion Engine Fundamentals*. McGraw-Hill Book Co, 1988.

[5] M. Jankovic, M. Jankovic, and I.V. Kolmanovsky. Constructive lyapunov control design for turbocharged diesel engines. *IEEE Transactions on Control Systems Technology*, 2000.

[6] Andreas Jerhammar and Erik Höckerdal. Gas flow observer for a Scania diesel engine with VGT and EGR. Master's thesis, Linköpings Universitet, SE-581 83 Linköping, 2006.

[7] I.V. Kolmanovsky, A.G. Stefanopoulou, P.E. Moraal, and M. van Nieuwstadt. Issues in modeling and control of intake flow in variable geometry turbocharged engines. In *Proceedings of* 18^{th} *IFIP Conference on System Modeling and Optimization*, Detroit, July 1997.

[8] M. Nieuwstadt, P.E. Moraal, I.V. Kolmanovsky, A. Stefanopoulou, P. Wood, and M. Widdle. Decentralized and multivariable designs for EGR–VGT control of a diesel engine. In *IFAC Workshop, Advances in Automotive Control*, 1998.

[9] M.J. Nieuwstadt, I.V. Kolmanovsky, P.E. Moraal, A.G. Stefanopoulou, and M. Jankovic. EGR–VGT control schemes: Experimental comparison for a high-speed diesel engine. *IEEE Control Systems Magazine*, 2000.

[10] R. Rajamani. Control of a variable-geometry turbocharged and wastegated diesel engine. *Proceedings of the I MECH E Part D Journal of Automobile Engineering*, November 2005.

[11] J. Rückert, A. Schloßer, H. Rake, B. Kinoo, M. Krüger, and S. Pischinger. Model based boost pressure and exhaust gas recirculation rate control for a diesel engine with variable turbine geometry. In *IFAC Workshop: Advances in Automotive Control*, 2001.

[12] A.G. Stefanopoulou, I.V. Kolmanovsky, and J.S. Freudenberg. Control of variable geometry turbocharged diesel engines for reduced emissions. *IEEE Transactions on Control Systems Technology*, 8(4), July 2000.

[13] Johan Wahlström. Control of EGR and VGT for emission control and pumping work minimization in diesel engines. Licentiate Thesis, Linköping University, 2006.

[14] Johan Wahlström, Lars Eriksson, and Lars Nielsen. Controller tuning based on transient selection and optimization for a diesel engine with EGR and VGT. In *Electronic Engine Controls*, number 2008-01-0985 in SAE Technical paper series SP-2159, SAE World Congress, Detroit, USA, 2008.

[15] Johan Wahlström and Lars Eriksson. Modeling of a diesel engine with VGT and EGR capturing sign reversal and non-minimum phase behaviors. Technical report, Linköping University, 2009.

[16] Johan Wahlström, Lars Eriksson, and Lars Nielsen. System analysis of a diesel engine with VGT and EGR. Technical report, Linköping University, 2009.

[17] K. J. Åström and T. Hägglund. *PID Controllers: Theory, Design and Tuning*. Research Triangle Park, Instrument Society of America, 2nd edition, 1995.